Influence of the Third Invariant in the Ballistic Impact of Silicon Carbide

Prepared by

Stephen R. Beissel
Timothy J. Holmquist
Gordon R. Johnson

Southwest Research Institute
5353 Wayzata Boulevard
Suite 607
Minneapolis, MN 55416

Contract W56HZV-06-C-0194

SwRI Report 18.12544/024

Prepared for:

US Army RDECOM-TARDEC
RDTA-RS
Warren, MI 48397-5000

August 2010

REPORT DOCUMENTATION PAGE

Form Approved
OMB No. 0704-0188

Public reporting burden for this collection of information is estimated to average 1 hour per response, including the time for reviewing instructions, searching data sources, gathering and maintaining the data needed, and completing and reviewing the collection of information. Send comments regarding this burden estimate or any other aspect of this collection of information, including suggestions for reducing this burden to Washington Headquarters Service, Directorate for Information Operations and Reports, 1215 Jefferson Davis Highway, Suite 1204, Arlington, VA 22202-4302, and to the Office of Management and Budget, Paperwork Reduction Project (0704-0188) Washington, DC 20503.

PLEASE DO NOT RETURN YOUR FORM TO THE ABOVE ADDRESS.

1. REPORT DATE *(DD-MM-YYYY)*
06-08-2010

2. REPORT TYPE
Technical

3. DATES COVERED *(From - To)*
6/09 -8/10

4. TITLE AND SUBTITLE
Influence of the Third Invariant in the Ballistic Impact of Silicon Carbide

5a. CONTRACT NUMBER
W56HZV-06-C-0194

5b. GRANT NUMBER

5c. PROGRAM ELEMENT NUMBER

6. AUTHOR(S)
Stephen R. Beissel, Timothy J. Holmquist and Gordon R. Johnson

5d. PROJECT NUMBER
18.12544

5e. TASK NUMBER

5f. WORK UNIT NUMBER

7. PERFORMING ORGANIZATION NAME(S) AND ADDRESS(ES)
Southwest Research Institute
5353 Wayzata Blvd., Suite 607
Minneapolis, MN 55416

8. PERFORMING ORGANIZATION REPORT NUMBER
18.12544/024

9. SPONSORING/MONITORING AGENCY NAME(S) AND ADDRESS(ES)
US Army Tank-Automotive Research, Development, and Engineering Center,
Warren, MI 48397-5000

10. SPONSOR/MONITOR'S ACRONYM(S)
RDECOM-TARDEC/RDTA-RS

11. SPONSORING/MONITORING AGENCY REPORT NUMBER

12. DISTRIBUTION AVAILABILITY STATEMENT
Approved for Public Release; Unlimited Distribution

13. SUPPLEMENTARY NOTES
The views, opinion, and/or findings contained in this report are those of the authors and should not be construed as an official Department of the Army position, policy, or decision, unless so designated by other documents.

14. ABSTRACT

This report examines the dependence of the ballistic performance of silicon carbide on the third invariant of the stress tensor by use of numerical simulations and test data. The JHB ceramic model is modified to account for the influence of the third invariant, and the modification includes a material parameter defined as the ratio of yield in tri-axial extension to yield in tri-axial compression. Simulations of high-velocity impact are performed systematically with several values of the parameter to determine the influence of the third invariant. The simulation results are also compared to test data to determine the degree of influence that provides the best agreement. Simulations include tensile and compressive plate-impact tests, long-rod penetration of prestressed targets, long-rod penetration of confined targets, long-rod penetration of unconfined targets, and ballistic impact of thin targets with substrates.

15. SUBJECT TERMS
silicon carbide, third invariant, ceramic constitutive modeling, JHB model, impact

16. SECURITY CLASSIFICATION OF:
Unclassified, Limited Distribution

a. REPORT	**b. ABSTRACT**	**c. THIS PAGE**	**17. LIMITATION OF ABSTRACT**	**18. NUMBER OF PAGES**
Limited	Unlimited	Unlimited	None	40

19a. NAME OF RESPONSIBLE PERSON
Frederick C. Rickert

19b. TELEPHONE NUMBER (*Include area code*)
586-282-3914

Table of Contents

Page

1.0 Introduction 1

2.0 The JHB Ceramic Model 3

  2.1 Original Form 3

  2.2 Incorporation of the Third Invariant 4

  2.3 Parameters for Silicon Carbide 6

3.0 Computed Results 9

  3.1 Compressive Plate Impact 9

  3.2 Tensile-Spall Plate Impact 10

  3.3 Prestressed Long-Rod Penetration 11

  3.4 Confined Long-Rod Penetration 13

  3.5 Unconfined Long-Rod Penetration 14

  3.6 Thin Target with Substrate 15

4.0 Discussion and Conclusions 17

5.0 References 19

Appendix A: Damage Softening A-1

Appendix B: Thermal Softening B-1

List of Figures and Table

Page

Figure 1. Dependence of tri-axial compressive yield strength on pressure in the JHB ceramic model. Undamaged ceramic is governed by the top curve, and fully damaged ceramic is governed by the bottom curve. Model parameters p_i, σ_i, σ_{max} ant T are shown for undamaged ceramic.............. 4

Figure 2. Effect of the tri-axial yield ratio Ψ on the yield surface, as seen in a plane normal to the line $\sigma_1 = \sigma_2 = \sigma_3$ in principal stress space for high pressures (left) and low pressures (right). θ is the Lode angle 6

Figure 3. Redefinition of the linear part of the JHB tri-axial compressive yield curve for variations in Ψ. Redefinition is necessary to maintain model agreement with spall data.. 7

Figure 4. Compressive plate-impact results from tests [10] and simulations for several values of Ψ and impact velocities of 1566 m/s (top) and 2259 m/s (bottom). Velocities are at the back surface of the silicon carbide 10

Figure 5. Tensile-spall plate-impact results from the test [11] and simulations for several values of Ψ at an impact velocity of 148 m/s. Velocities are at the back surface of the silicon carbide 11

Figure 6. Results of tungsten long-rod impacts with thick prestressed silicon-carbide targets from tests [12] and simulations for several values of Ψ. Test data are indicated by squares (1410 m/s), diamonds (1645 m/s) and triangles (2175 m/s).. 12

Figure 7. Contours of sin(3θ) at 10 μs (left) and 20 μs (right) from the simulation of a long rod impact with a prestressed silicon-carbide target at 1645 m/s and $\Psi = 0.5$. Values of sin(3θ) near tri-axial compression are shaded dark gray; those near tri-axial extension are shaded white 12

Figure 8. One-standard-deviation error bars of the penetration depths from simulations of long-rod impacts with confined silicon-carbide targets for several values of Ψ. .Each error bar represents five simulations, and two of them are shifted horizontally at each impact velocity to help distinguish them visually. The error bar from $\Psi = 1$ is on the left of each trio, and that from $\Psi = 0.5$ is on the right 13

Figure 9. Penetration velocities of long-rod impacts with unconfined silicon-carbide targets from tests [15] and simulations using several values of Ψ 14

List of Figures and Table (Cont'd)

Page

Figure 10. Simulation results of bullets impacting thin targets of silicon carbide and aluminum: bullet residual velocities for several values of Ψ (top) and contours of pressure (bottom left) and sin(3θ) (bottom right) from the simulation with Ψ = 0.5 and impact velocity of 740 m/s.......................... 15

Figure A-1. Compressive plate-impact results from tests [10] and simulations for several degrees of damage softening and impact velocities of 1566 m/s (top) and 2259 m/s (bottom). Velocities are from the back surface of the silicon carbide A-2

Figure A-2. Tensile-spall plate-impact results from the test [11] and simulations for several degrees of damage softening and an impact velocity of 148 m/s. Velocities are at the back surface of the silicon carbide A-3

Figure A-3. Results of tungsten long-rod impacts with thick prestressed silicon-carbide targets from tests [12] and simulations for several degrees of damage softening. Test data are indicated by squares (1410 m/s), diamonds (1645 m/s) and triangles (2175 m/s) A-3

Figure A-4. Penetration depths from simulations of long-rod impacts with confined silicon-carbide targets for several degrees of damage softening A-4

Figure A-5. Penetration velocities of long-rod impacts with unconfined silicon-carbide targets from tests [15] and simulations for several degrees of damage softening A-4

Figure A-6. Residual velocities from simulations of bullets impacting thin targets of silicon carbide and aluminum for several degrees of damage softening ... A-5

Figure B-1. Compressive plate-impact results from tests [10] and simulations with and without thermal softening at impact velocities of 1566 m/s (top) and 2259 m/s (bottom). Velocities are from the back surface of the silicon carbide B-2

Figure B-2. Tensile-spall plate-impact results from the test [11] and simulations with and without thermal softening at an impact velocity of 148 m/s. Velocities are at the back surface of the silicon carbide B-3

List of Figures and Table (Cont'd)

Page

Figure B-3. Results of tungsten long-rod impacts with thick prestressed silicon-carbide targets from tests [12] and simulations with and without thermal softening. Test data are indicated by squares (1410 m/s), diamonds (1645 m/s) and triangles (2175 m/s) B-4

Figure B-4. Penetration depths from simulations of long-rod impacts with confined silicon-carbide targets with and without thermal softening B-4

Figure B-5. Penetration velocities of long-rod impacts with unconfined silicon-carbide targets from tests [15] and simulations with and without thermal softening B-5

Figure B-6. Residual velocities from simulations of bullets impacting thin targets of silicon carbide and aluminum with and without thermal softening B-6

Table 1. Values of silicon-carbide yield-surface parameters that depend on Ψ 7

1.0 Introduction

Concrete and engineering ceramics exhibit similarities at both the microscopic and macroscopic levels. They are both covalently bonded polycrystalline materials with yield strengths and ductilities that are strongly dependent on pressure. At low pressures, they fail in brittle fracture at relatively small loads; and at high pressures, they remain elastic to much larger loads, and incur relatively large inelastic strains before failure. In addition, the mechanical behavior of concrete is known to depend upon the third invariant of the stress tensor [1-3]. Although engineering ceramics are more homogeneous and less porous than concrete, the mechanical and microstructural similarities of these two classes of materials raise the question whether the mechanical behavior of ceramics is also dependent upon the third invariant of the stress tensor. This report examines the possibility that the yield surface of silicon carbide, a ceramic commonly used in armor applications, is dependent upon the third invariant.

Traditional techniques for measuring yield stresses at high pressures, such as tri-axial loading, are limited by the very high strength of silicon carbide at high pressures. As a result, the best means of evaluating silicon-carbide strength characteristics at high pressures is often by high-velocity impact. In this report, tests of high-velocity impact are selected from the literature for investigating the influence of the third invariant. The tests are each simulated numerically with several values of the tri-axial yield ratio, a material parameter defined as the ratio of yield in tri-axial extension to yield in tri-axial compression. The simulation results indicate the sensitivity of each test to silicon carbide's dependence on the third invariant. In addition, comparison of the test and simulation results suggests the actual magnitude of silicon carbide's dependence on the third invariant.

In the simulations, the JHB ceramic model [4] is used to describe the mechanical behavior of silicon carbide. This model was formulated specifically to address the conditions resulting from high-velocity impact: large strains at high pressures and strain rates. Since the model does not include the influence of the third invariant, it has been augmented for the simulations in this report by a factor dependant upon the third invariant. Several such factors have been proposed for concrete and geomaterials, e.g. Mohr-Coulomb [5], Willam-Warnke [6] and Gudehus [7], each of which depends upon the tri-axial yield ratio. Here, the factor introduced by Gudehus is incorporated into the JHB model. In addition, several of the original JHB yield parameters are re-calibrated for each value of the tri-axial yield ratio in order to maintain agreement with the silicon-carbide test data. This process, along with a description of the model and the Gudehus factor, is described in the next section. Simulation and test results are presented in the subsequent section, followed by a discussion of the results. Two appendices are included documenting the influence on silicon carbide of damage softening and thermal softening, two additional characteristics for which the JHB model has been modified.

2.0 The JHB Ceramic Model

2.1 Original Form

The JHB model was introduced [4] to describe the behavior of ceramics under the conditions of ballistic impact: large strains at high strain rates and pressures. In its original form, the model describes the yield surface as,

$$\sigma = \sigma_{TXC}(p;D)(1 + C\ln\dot{\varepsilon}^*) \tag{1}$$

In this equation, σ is the equivalent stress, $\sigma = \sqrt{3J_2}$, where $J_2 = \underline{s} : \underline{s}/2$ is the second invariant of the stress deviator, $\underline{s}$. On the right side, p is the pressure; D is the damage; $\dot{\varepsilon}^*$ is the dimensionless strain rate; and $\sigma_{TXC}(p;D)$ is the isothermal tri-axial compressive strength at $\dot{\varepsilon}^* = 1.0$. The factor $(1 + C\ln\dot{\varepsilon}^*)$, including material parameter C, accounts for the influence of the strain rate. Since the state of stress is only represented by its first and second invariants (scaled to p and σ, respectively), the original form of the JHB model does not account for effects of the third invariant.

The function $\sigma_{TXC}(p;D)$ takes the following form.

$$\sigma_{TXC}(p;D) = \begin{cases} \dfrac{\sigma_i(p+T)}{(p_i+T)} & for\ \ -T \le p \le p_i \\ \sigma_i + (\sigma_{\max} - \sigma_i)\left\{1 - \exp\left[\dfrac{-\sigma_i(p-p_i)}{(p_i+T)(\sigma_{\max}-\sigma_i)}\right]\right\} & for\ \ p > p_i \end{cases} \tag{2}$$

This equation breaks the function into two parts: a linear function for $-T \le p \le p_i$, and an exponential function for $p > p_i$. The two functions and their derivatives are continuous at their interface, point (p_i, σ_i). The model parameters are p_i, σ_i, the asymptotic limit of the strength for large pressures, $\sigma_{\max}$, and the tensile (negative) pressure at which strength vanishes, T. These parameters are shown graphically in Fig. 1 for the yield surface of undamaged material, denoted by $\sigma_{TXC}(p;D=0)$.

The dependence of $\sigma_{TXC}(p;D)$ on damage D occurs through the model parameters. In addition to the set of parameters depicted in Fig. 1 for the yield surface of undamaged material, another set defines the yield surface of fully damaged material, denoted by $\sigma_{TXC}(p;D=1)$. When loading reaches the undamaged yield surface, the material incurs plastic strains and damage from further loading each timestep n.

$$D = \sum_n \frac{\Delta\varepsilon_p(t_n)}{\varepsilon_{pf}(p,t_n)} \tag{3}$$

In this expression, $\Delta\varepsilon_p(t_n)$ is the increment in plastic strain during timestep n, and $\varepsilon_{pf}(p,t_n)$ is the plastic strain to failure under the conditions at t_n,

$$\varepsilon_{pf}(p, t_n) = D_1 \left(\frac{p + T}{\sigma_{\max}} \right)^N \tag{4}$$

Here D_1 and N are model parameters.

Because it is difficult to measure damage, there is some uncertainty about the strength of partially damaged ($0 < D < 1$) ceramics. In the JHB model, the strength of partially damaged material is governed by the undamaged yield surface. When damage is complete ($D = 1$), the strength is then governed by the damaged yield surface. The transition between these two yield surfaces is depicted in Fig. 1 by the dashed line indicating instantaneous softening when $D = 1$. An alternate approach to modeling the strength of partially damaged material is shown by the dashed line indicating gradual softening when $D > 0$.

The volumetric response of the ceramic is expressed as,

$$p = \mathrm{K}_1 \mu + \mathrm{K}_2 \mu^2 + \mathrm{K}_3 \mu^3 + \Delta p \tag{5}$$

In this expression, μ is the compressibility (ratio of reduction in volume to initial volume); Δp is the increment in pressure due to bulking; and K_1, K_2 and K_3 are model parameters.

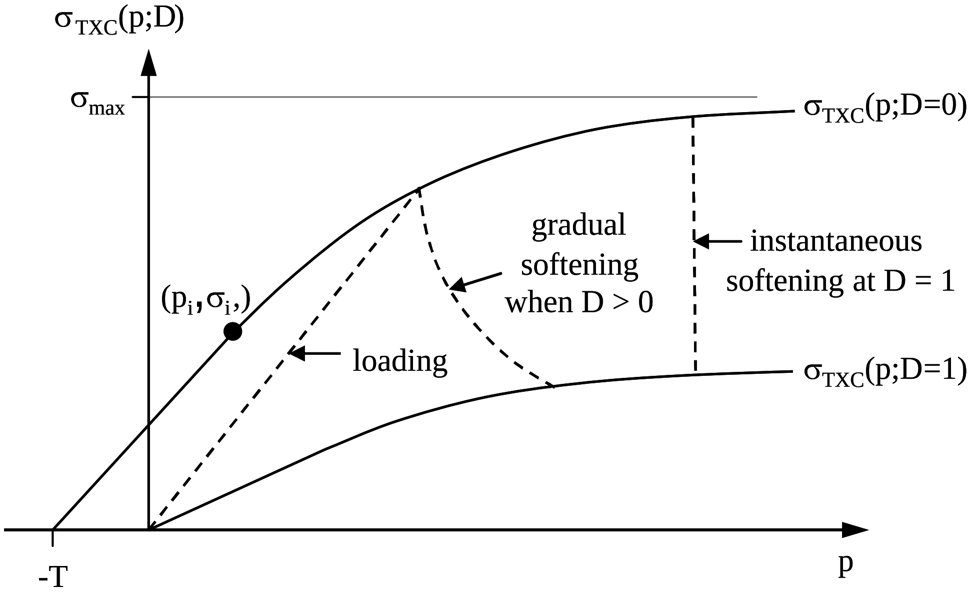
σTXC(p;D)
σmax
σTXC(p;D=0)
gradual softening when D > 0
instantaneous softening at D = 1
(pi,σi,)
loading
σTXC(p;D=1)
-T
p

Figure 1. Dependence of tri-axial compressive yield strength on pressure in the JHB ceramic model. Undamaged ceramic is governed by the top curve, and fully damaged ceramic is governed by the bottom curve. Model parameters p_i, σ_i, σ_{max} and T are shown for undamaged ceramic.

2.2 Incorporation of the Third Invariant

Equation 1 expresses the yield surface in terms of the first and second stress invariants. For the incorporation of the third invariant, principal-stress space provides a useful context because every stress state can be uniquely defined by its three invariants. In principal-stress space, the first and second invariants represent the line $\sigma_1 = \sigma_2 = \sigma_3$ and the radial distance from that line, respectively. The portion of the third invariant that is independent of the first and second invariants must therefore represent the angular coordinate of a cylindrical coordinate system with axis $\sigma_1 = \sigma_2 = \sigma_3$ in principal-stress space. The Lode angle θ is such an angular coordinate, and it is related to the second and third invariants of the stress deviators (J_2 and J_3) by the relation [8],

$$\sin(3\theta) = \frac{J_3}{2}\left(\frac{3}{J_2}\right)^{3/2} \tag{6}$$

With Lode angle θ as the independent variable, the influence of the third stress invariant can be introduced into the JHB model by appending factor $\Gamma(\theta;\Psi)$ to equation 1:

$$\sigma = \sigma_{TXC}(p;D)\,(1 + C\ln\dot{\varepsilon}^*)\,\Gamma(\theta;\Psi) \tag{7}$$

Parameter Ψ is the ratio of yield strength in tri-axial extension to yield in tri-axial compression, and the factor $\Gamma(\theta;\Psi)$ scales the tri-axial compressive strength for other stress states. The form of $\Gamma(\theta;\Psi)$ introduced by Gudehus [7] is used in this study.

$$\Gamma(\theta;\Psi) = \frac{\Psi}{2}\left\{1 + \sin(3\theta) + \frac{1}{\Psi}\left[1 - \sin(3\theta)\right]\right\} \tag{8}$$

The left side of Fig. 2 shows the effect of $\Gamma(\theta;\Psi)$ on the yield surface in principal-stress space for large pressures when $\Psi = 1.0$, $\Psi = 0.75$ and $\Psi = 0.5$. The view is of a plane normal to the line $\sigma_1 = \sigma_2 = \sigma_3$, in which Lode angle θ is the angular coordinate, and the curves are the intersections of the yield surfaces with the plane. The curve denoted by $\Psi = 1.0$ is a circle, indicating that $\Gamma(\theta;\Psi = 1.0) = 1$ for all θ, and strength is independent of the third invariant. This curve represents the original form of the JHB model, as Eqn. 7 reduces to Eqn. 1 when $\Gamma = 1$. The curves denoted by $\Psi = 0.75$ and $\Psi = 0.5$ demonstrate successively greater influence of the third invariant. For $\theta = -30^\circ$, the stress state is tri-axial compression ($\sigma_1 = \sigma_2 > \sigma_3$), $\Gamma(-30^\circ;\Psi) = 1.0$, and the curves coincide for all values of Ψ. For $\theta = 30^\circ$, the stress state is tri-axial extension ($\sigma_1 > \sigma_2 = \sigma_3$), $\Gamma(30^\circ;\Psi) = \Psi$, and the curves differ maximally. The intermediate case of $\theta = 0^\circ$ represents pure shear.

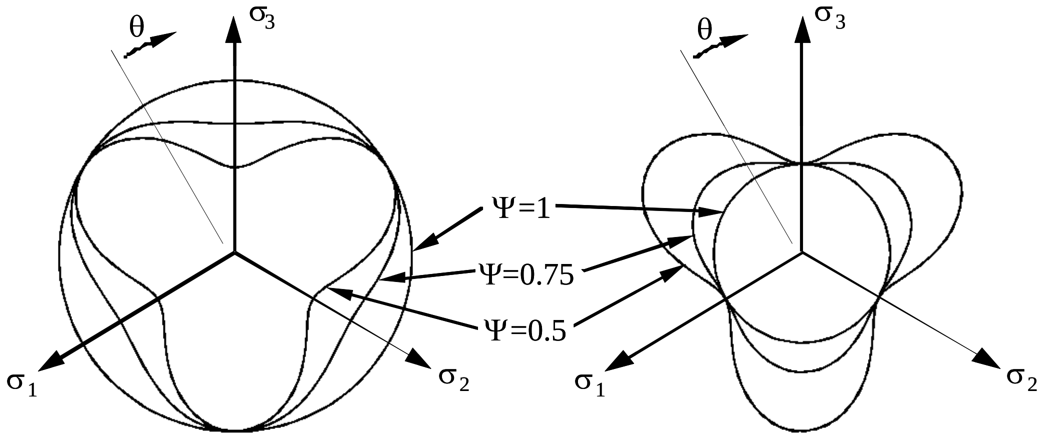

Figure 2. Effect of the tri-axial yield ratio Ψ on the yield surface, as seen in a plane normal to the line $\sigma_1 = \sigma_2 = \sigma_3$ in principal stress space for high pressures (left) and low pressures (right). θ is the Lode angle.

2.3 Parameters for Silicon Carbide

To examine the influence of the third invariant in silicon carbide, simulations of plate-impact and ballistic tests are compared to test data in the following section. The simulations are performed with $\Psi = 1.0$, $\Psi = 0.75$ and $\Psi = 0.5$ to identify trends in the influence of the third invariant.

The yield surface of undamaged material in tri-axial compression, denoted by $\sigma_{TXC}(p; D = 0)$ in Fig. 1, is defined by parameters p_i, σ_i, $\sigma_{\max}$ and T. These parameters are unique to each ceramic and they are generally determined by best agreement with compressive and spall plate-impact and Hopkinson-bar test data. Since each of these tests involves high strain rates, the term $(1 + C \ln \dot{\varepsilon}^*)$ in Eqn. 7 must be factored into the determination of the parameters. In similar fashion, the term $\Gamma(\theta; \Psi)$ must be factored into the determination when $\Psi < 1.0$, i.e., the influence of the third invariant is nonzero. One consequence of this coupling is that the parameters that best agree with the test data depend in general upon the value of Ψ.

Since $\Gamma = 1.0$ for all values of Ψ when the state of stress is tri-axial compression, and Γ varies with Ψ for other states of stress, the parameters p_i, σ_i, $\sigma_{\max}$ and T will depend upon Ψ only when they are derived from tests in which the state of stress is not tri-axial compression at yield. In the compressive plate-impact and Hopkinson-bar tests, the state of stress at yield is indeed tri-axial compression. Due to the high pressures in these tests, their data are generally used to determine the exponential part of Eqn. 2, which governs when $p > p_i$. However, in the spall plate-impact tests, the state of stress at yield is tri-axial extension. Since the pressure is negative (tensile) in these tests, their data are used to determine the linear part of Eqn. 2, which governs when $-T \le p \le p_i$. Therefore, the parameters defining the linear part of Eqn. 2 (p_i, σ_i and T) must be redefined for each value of Ψ to ensure that the model agrees with the spall tests. But the parameters defining the exponential part of Eqn. 2 are effectively independent of Ψ.

The linear parts of Eqn. 2 corresponding to each of the three values of Ψ are depicted by the solid lines in Fig. 3. These lines represent yield in tri-axial compression such that the corresponding yield in tri-axial extension passes through the spall data. These lines are tangent to the same exponential curve at different points. Yield in tri-axial extension is depicted by the dashed and dotted lines in Fig. 3 for $\Psi = 0.75$ and $\Psi = 0.5$, respectively, and it is attained by multiplying the yield in tri-axial compression by $\Gamma(30^\circ;\Psi) = \Psi$. The effect of redefining the yield surface to retain agreement with the spall data for each values of Ψ is also depicted on the right side of Fig. 2, where the yield surfaces intersecting a plane normal to the line $\sigma_1 = \sigma_2 = \sigma_3$ can be seen to coincide for tri-axial extension.

In the simulations reported in the following section, the JHB model parameters used for silicon carbide are those derived by Holmquist and Johnson [9] for SiC-B, except for the values of p_i, σ_i and T that are used when $\Psi = 0.75$ and $\Psi = 0.5$. Those values are shown in Table 1, along with the values of p_i, σ_i and T reported by Holmquist and Johnson [9] and used when $\Psi = 1.0$.

Table 1. Values of silicon-carbide yield-surface parameters that depend on Ψ

	$\Psi = 1.0$	$\Psi = 0.75$	$\Psi = 0.5$
p_i (GPa)	1.50	1.67	2.01
σ_i (GPa)	4.92	5.28	5.95
T (GPa)	0.750	0.876	1.163

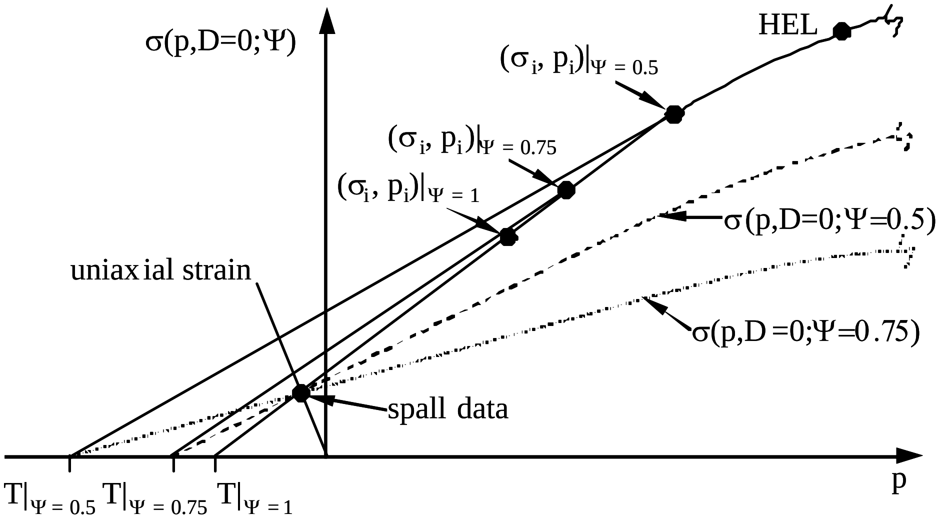
σ(p,D=0;Ψ)
HEL
$(\sigma_i, p_i)|_{\Psi = 0.5}$
$(\sigma_i, p_i)|_{\Psi = 0.75}$
$(\sigma_i, p_i)|_{\Psi = 1}$
σ(p,D=0;Ψ=0.5)
uniaxial strain
σ(p,D=0;Ψ=0.75)
spall data
p
$T|_{\Psi = 0.5}$ $T|_{\Psi = 0.75}$ $T|_{\Psi = 1}$

Figure 3. Redefinition of the linear part of the JHB tri-axial compressive yield curve for variations in Ψ. Redefinition is necessary to maintain model agreement with spall data.

3.0 Computed Results

In this section, the results from simulations of high-velocity impacts with silicon-carbide targets are reported for several values of the ratio of yield in tri-axial compression to yield in tiraxial extension ($\Psi = 1.0$, $\Psi = 0.75$ and $\Psi = 0.5$), and the results are compared to test data from the literature. The tests include tensile and compressive plate impacts, long-rod penetration of several thick targets, and ballistic impact of thin targets with substrates. Simulations of these tests have been reported by Holmquist and Johnson for $\Psi = 1.0$ [9], and the same numerical algorithms and initial finite-element meshes are used here. Plate impact simulations are performed in uniaxial strain, and all other simulations are performed in two-dimensional axisymmetry. Further details of the meshes are included in their paper [9].

3.1 Compressive Plate Impact

Figure 4 shows the results from tests and simulations of two compressive plate impacts: at 1566 m/s on the top, and 2259 m/s on the bottom. The impacting plate is silicon carbide, and the target plate is silicon carbide on the impacted side and lithium fluoride on the back side. The plots compare the computed histories of silicon-carbide velocity at its interface with the lithium fluoride to the VISAR test results of Grady and Moody [10]. Simulation results are indicated by a line of long dashes for $\Psi = 1.0$, a line of short dashes for $\Psi = 0.75$, and a dotted line for $\Psi = 0.5$; test results are indicated by a solid line.

Because the state of stress in the silicon carbide is tri-axial compression throughout loading and until it switches to tri-axial extension during the elastic part of unloading, the three computed results are identical until the material reaches yield in tri-axial extension. Due to the different values of Ψ, the computed results have different yield points in tri-axial extension. This is seen by divergence of the three computed results at the end of the steeply downward-sloping part of the velocity histories. Yield is indicated by an abrupt transition to a milder downward slope. For both impact velocities, the results from $\Psi = 0.5$ first diverge from the other two computed results because their yield in tri-axial extension is smallest. The results from $\Psi = 0.75$ are next to make the transition, as they represents the next weakest material in tri-axial extension.

In comparing the computed results to those from the test data, the transition indicating yield in tri-axial extension is best replicated at both impact velocities by the simulations using $\Psi = 0.5$. Further examination of the velocity histories after this transition indicate very good agreement between the simulations using $\Psi = 0.5$ and the test data. Agreement with test data diminishes for the simulations using $\Psi = 0.75$ and $\Psi = 1.0$.

In these simulations of compressive plate-impact tests, pressure remains positive as the material unloads and yields in tri-axial extension. As a result, the computations compute yield in tri-axial extension by factoring the exponential part of the yield function in Eqn. 2. Since this part is the same for each of the computations (independent of Ψ), yield in tri-axial extension diminishes with diminishing Ψ, as depicted on the left side of Fig. 2.

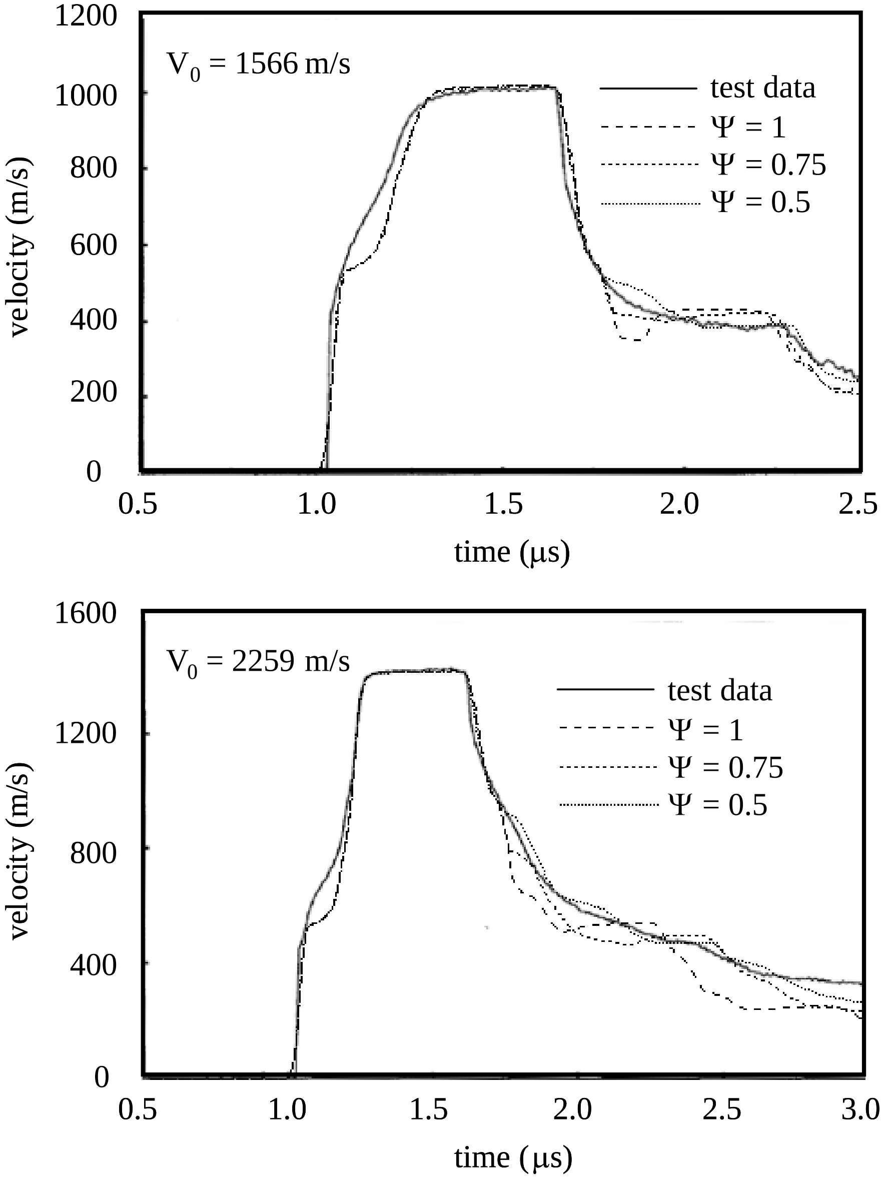

Figure 4. Compressive plate-impact results from tests [10] and simulations for several values of Ψ and impact velocities of 1566 m/s (top) and 2259 m/s (bottom). Velocities are at the back surface of the silicon carbide.

3.2 Tensile-Spall Plate Impact

Figure 5 shows the results from a test and simulations of a tensile-spall plate impact at 148 m/s. Both the impacting and target plates are silicon carbide, and the plot compares the computed velocities on the back side of the target plate to the VISAR data of Dandekar and Bartkowski [11].

Unlike the simulations of compressive plate-impact tests, the pressure in tensile-spall plate impact tests becomes negative as the material unloads and yields in tri-axial extension. As a result, the simulations compute yield in tri-axial extension by factoring the linear part of the yield function in Eqn. 2. This part differs for each value of Ψ in order to maintain the same yield stress in the state of tri-axial extension at spall, as shown in Fig. 3 and the right side of Fig. 2. The agreement of the three simulated results in Fig. 5 is therefore confirmation of the material parameters of Table 1, as they were derived to all agree with the spall data.

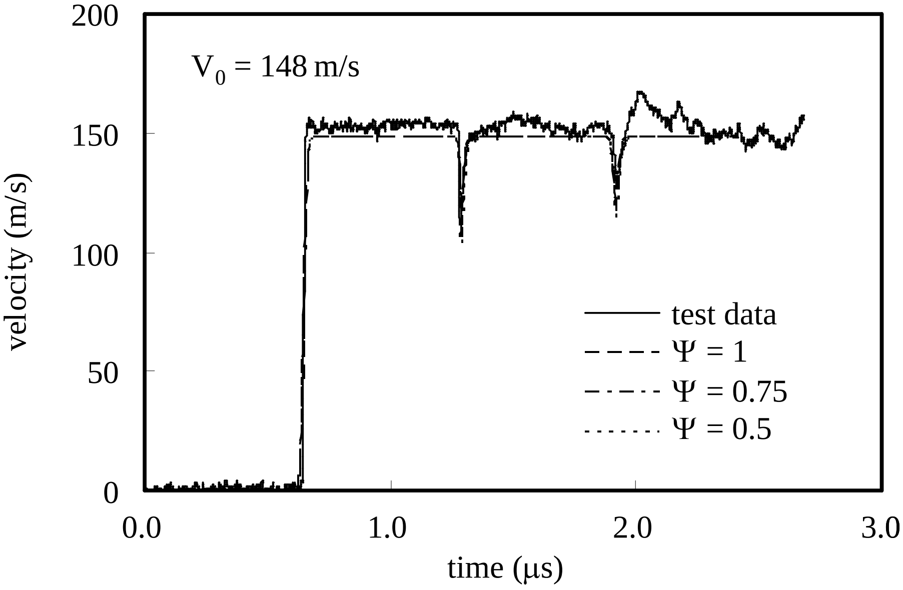

Figure 5. Tensile-spall plate-impact results from the test [11] and simulations for several values of Ψ at an impact velocity of 148 m/s. Velocities are at the back surface of the silicon carbide.

3.3 Prestressed Long-Rod Penetration

In the tests of Lundberg *et al* [12], silicon-carbide targets were prestressed by confinement and impacted with long stationary tungsten rods. Prestressing was achieved by heating the steel confining tube before inserting the cylinder of ceramic. Upon cooling, steel plugs were screwed tightly into the tube ends. Rings were then welded to the tube ends such that only the plugs act as cover plates along the target axis. During the tests, x-rays were taken at several times to determine penetration depths.

Figure 6 shows a comparison of silicon-carbide penetration versus time from three impact velocities. The test results are indicated by squares for the impact velocity of 1410 m/s, diamonds for 1645 m/s, and triangles for 2175 m/s. The simulations were performed with three values of Ψ for each impact velocity. They are represented by solid lines for $\Psi = 1.0$, long-dashed lines for $\Psi = 0.75$, and short-dashed lines for $\Psi = 0.5$. For the impact velocity of 1410 m/s, the rod dwells on the surface of the silicon carbide in the test, and in all three of the simulations. For the impact velocity of 2175 m/s, the rod shows negligible dwell and penetrates at a nearly constant velocity in the test and all three simulations. For the intermediate impact velocity of 1645 m/s, the rod dwells before penetrating. Although there is little difference between the results from the simulations with $\Psi = 1.0$ and $\Psi = 0.75$, the simulation with $\Psi = 0.5$ transitions from dwell to penetration about 3 μs sooner than the other two. The simulation with $\Psi = 1.0$ was used by Holmquist and Johnson [9] to determine the damage parameters D_1 and N in Eqn. 4. So for these simulations, agreement with the test data is not an indication of the most appropriate value of Ψ.

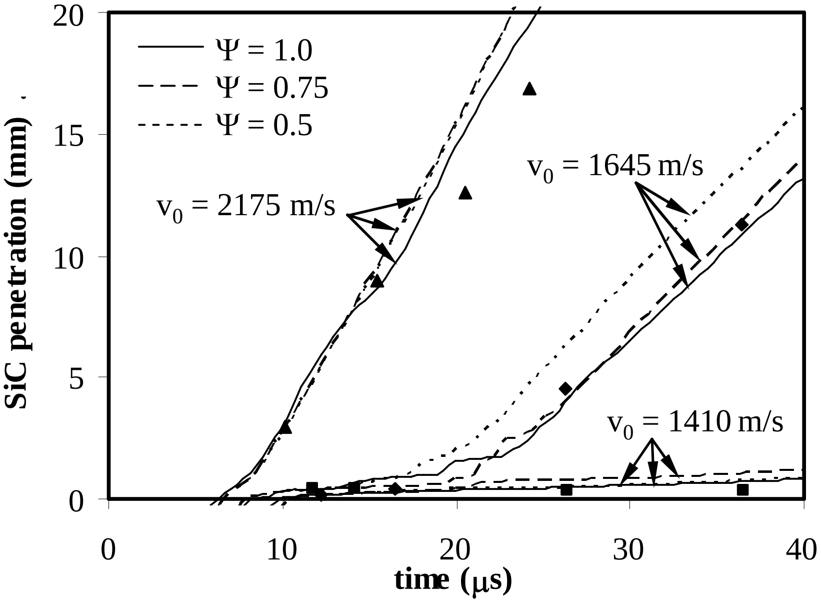

Figure 6. Results of tungsten long-rod impacts with thick prestressed silicon-carbide targets from tests [12] and simulations for several values of Ψ. Test data are indicated by squares (1410 m/s), diamonds (1645 m/s) and triangles (2175 m/s).

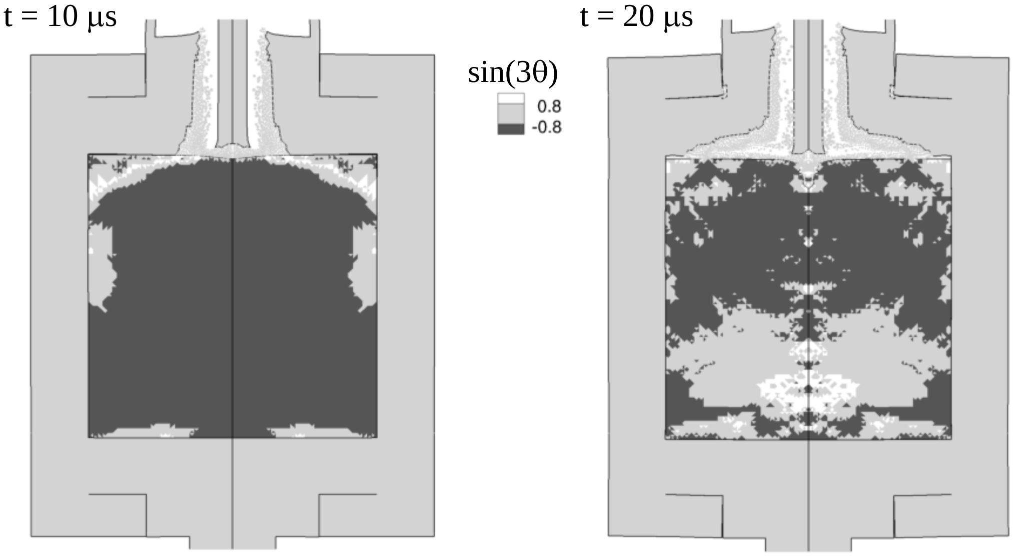

Figure 7. Contours of sin(3θ) at 10 μs (left) and 20 μs (right) from the simulation of a long-rod impact with a prestressed silicon-carbide target at 1645 m/s and Ψ = 0.5. Values of sin(3θ) near tri-axial compression are shaded dark gray; those near tri-axial extension are shaded white.

These simulations are useful, however, in demonstrating the influence of the third invariant on the very sensitive process of transitioning from dwell to penetration of a ceramic. The reduction in dwell of only 3 μs between $\Psi = 1.0$ and $\Psi = 0.5$ indicates little influence. Since the pressure is positive in the silicon carbide under the impact, the yield surfaces for the three values of Ψ are related as shown on the left side of Fig. 2, such that yield strengths are only similar near tri-axial compression. Therefore, the relative lack of influence of Ψ on the duration of dwell indicates that the silicon carbide under the impact must be predominantly in tri-axial compression. This conclusion is verified by the contour plots of $\sin(3\theta)$ in Fig. 7 from the simulation of the 1645-m/s impact velocity with $\Psi = 0.5$ at 10 μs and 20 μs. In these plots, stress states near tri-axial compression ($\sin(3\theta) \le -0.8$) are colored dark gray and they are affected very little by Ψ. Stress states near tri-axial extension ($\sin(3\theta) \ge 0.8$) are colored white and they are strongly affected by Ψ. Intermediate stress states are colored light gray. At 10 μs, the rod is dwelling and all of the silicon carbide under the impact is near tri-axial compression. At 20 μs, the rod has just begun penetration and the loading in a pocket of silicon carbide just below the impact is no longer near tri-axial compression.

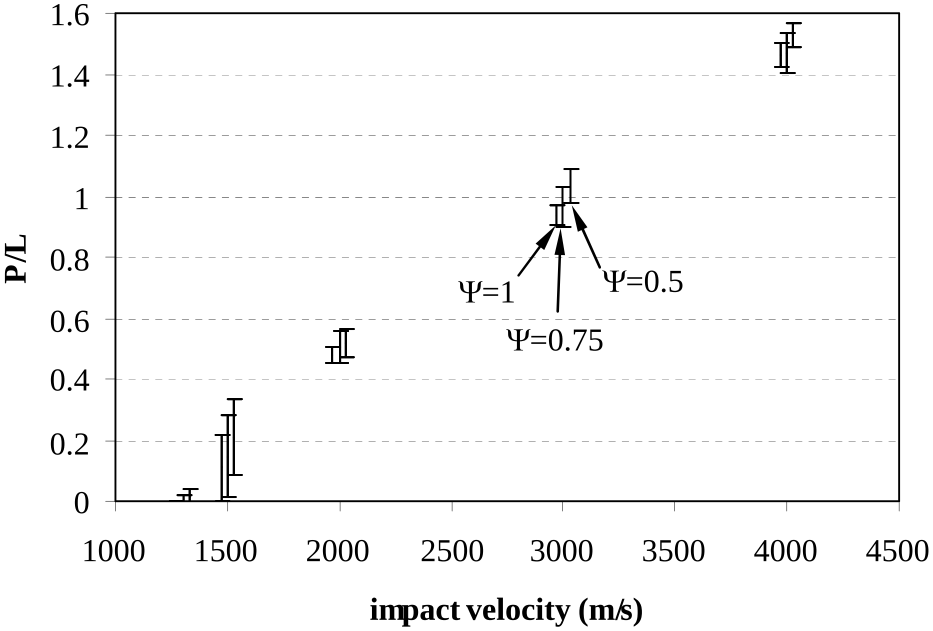

Figure 8. One-standard-deviation error bars of the penetration depths from simulations of long-rod impacts with confined silicon-carbide targets for several values of Ψ. Each error bar represents five simulations, and two of them are shifted horizontally at each impact velocity to help distinguish them visually. The error bar from Ψ = 1 is on the left of each trio, and that from Ψ = 0.5 is on the right.

3.4 Confined Long-Rod Penetration

In the tests of Orphal and Franzen [13], deep cylinders of silicon carbide were confined in titanium tubes with aluminum end plates. The cylinders were then impacted with long tungsten rods at velocities from about 1500 m/s to just under 5000 m/s. In this section, penetration depths are presented from simulations of the tests performed at impact velocities of 1300, 1500, 2000, 3000 and 4000 m/s for the three values of Ψ.

Both the tests and the simulations exhibit significantly more scatter in the total penetration than in the primary penetration, apparently due to the highly unstable afterflow. To gauge the influence of the third invariant, comparisons were therefore made of the penetration depths at 10 μs after impact, a time when primary penetration is nearly complete and no afterflow has occurred in any of the simulations. As a result, direct comparison to the test data is foregone in favor of less scatter in the results. However, this does not elmimate the scatter, as long-rod penetration of confined ceramics has been shown to be an inherently unsteady process [14] in both tests and computations. Therefore, five simulations were performed at 0.1-m/s intervals in each of the five impact velocities to determine the sensitivity of the penetration depths to very small perturbations. For example, statistics from simulations at 1999.8 m/s, 1999.9 m/s, 2000.0 m/s, 2000.1 m/s and 2000.2 m/s represent the impact velocity of 2000 m/s.

Figure 8 shows the penetration depths at 10 μs normalized by the original rod length, L. The five simulations performed for each value of Ψ and each impact velocity are represented by a one-standard-deviation error bar. In each trio of error bars, two are shifted horizontally by a small increment to help distinguish them visually, with the error bar from the simulations using $\Psi = 1.0$ on the left, that from $\Psi = 0.75$ in the center, and that from $\Psi = 0.5$ on the right. This plot indicates both the influence of the third invariant and the sensitivity to small perturbations in the impact velocity. For each of the impact velocities, the mean value of penetration depth (as indicated by the midpoint of the error bar) increases with decreasing Ψ. However, for impact velocities of 2000 m/s, 3000 m/s and 4000 m/s, the increases are small compared to the magnitudes of the penetration depths.

3.5 Unconfined Long-Rod Penetration

In the tests of Behner *et al* [15], unconfined silicon carbide was impacted onto stationary gold rods at velocities of 3502 m/s, 3944 m/s and 4462 m/s, and penetration velocities were determined from penetration depths recorded by x-rays. For this study, simulations are performed at the impact velocity of 4000 m/s with each value of Ψ, and the penetration velocities are determined analogously.

Figure 9 shows a comparison of the penetration velocities from the tests and simulations. The effect of the third invariant is small, and each of the simulations agrees well with the test data. Since simulations were not performed with perturbations in the initial conditions, it is not possible to determine their sensitivities. However, there is no clear trend in the influence of the third invariant.

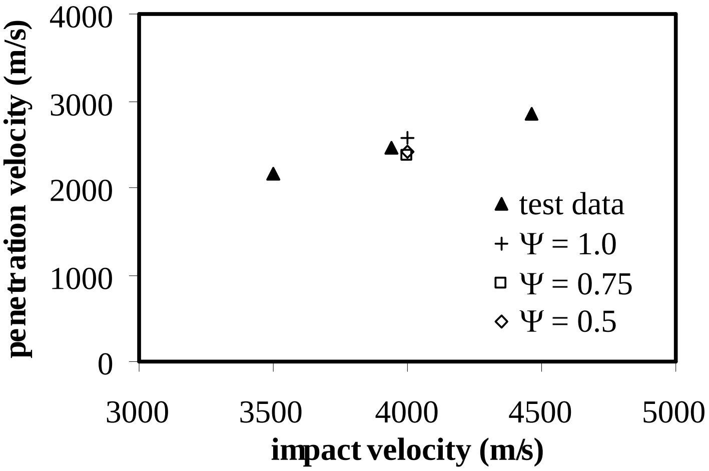

Figure 9. Penetration velocities of long-rod impacts with unconfined silicon-carbide targets from tests [15] and simulations using several values of Ψ.

3.6 Thin Target with Substrate

In the tests of Wilkins [16], 7.62-mm pointed-nose steel bullets were shot at targets of 6.35-mm silicon-carbide tiles over 6.35-mm aluminum plates, and a ballistic limit of 660 m/s was reported. In this study, simulations of these impacts are performed over a broad range of impact velocities at 4-m/s intervals for each value of Ψ.

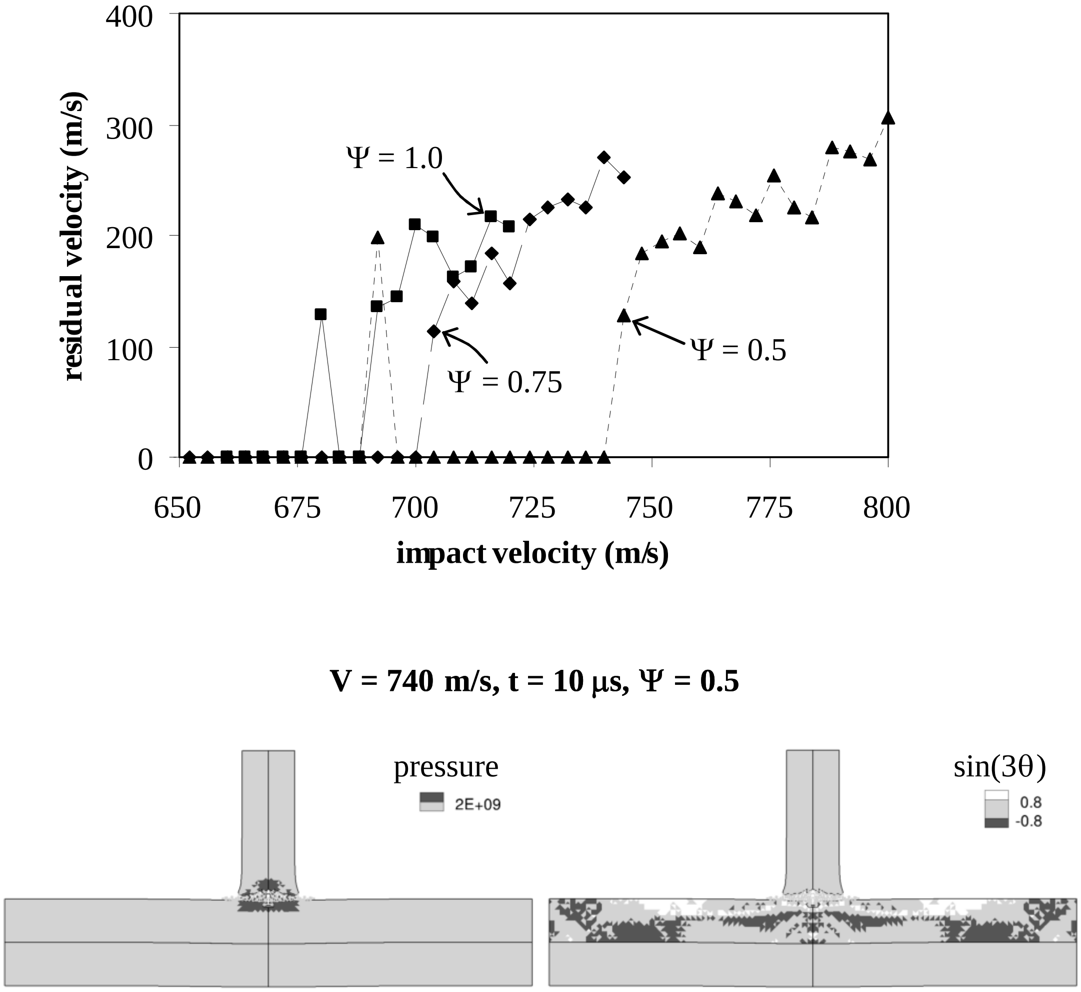

Figure 10. Simulation results of bullets impacting thin targets of silicon carbide and aluminum: bullet residual velocities for several values of Ψ (top) and contours of pressure (bottom left) and sin(3θ) (bottom right) from the simulation with Ψ = 0.5 and impact velocity of 740 m/s.

The top of Fig. 10 is a plot of the residual bullet velocities versus impact velocities from each of the simulations. The sensitivity of the residual velocities to variations in the impact velocities is reflected by the noise in the data, and by the velocity of the slowest complete penetration being less than that of the fastest incomplete penetration for both $\Psi = 1.0$ and $\Psi = 0.5$. Despite this sensitivity, the data show a clear trend toward higher ballistic limits with decreasing Ψ, as the ballistic limit with $\Psi = 0.5$ is at least 50 m/s greater than that with $\Psi = 1.0$. This trend indicates increasing silicon-carbide yield strength with decreasing Ψ. It is therefore the opposite trend of that from the thick targets of prestressed and confined silicon carbide of preceding sections. Referring to Fig. 2, increasing silicon-carbide yield strengths with decreasing Ψ occur only in the linear part of the curve ($-T \le p \le p_i$), where it is redefined (via parameters p_i, σ_i and T) to accommodate the spall data. The contour plots on the bottom of Fig. 10 verify that the stress states in the thin-target silicon carbide allow it to access these higher yield strengths as Ψ decreases. The plots are from the simulation with $\Psi = 0.5$ at an impact velocity of 740 m/s and 10 μs after impact. For this value of Ψ, yield at all pressures below $p_i = 2.0 GPa$ is governed by the linear part of the yield curve, which increases for decreasing Ψ. Pressures below $p_i = 2.0 GPa$ are colored light gray in the contour plot on the left. Only a small region of the silicon carbide just beneath the impact has higher pressure. In addition, the plot on the right shows contours of $\sin(3\theta)$, and it indicates that most of the silicon carbide is near tri-axial compression or intermediate with tri-axial extension.

The silicon carbide tested by Wilkins was KT-SiC [16], not the hot-pressed SiC-B modeled in these simulations. The KT-SiC was of lesser density and lower Hugoniot elastic limit, and therefore likely of lesser ballistic resistance. As a result, the ballistic limit from the simulations should be greater than the 660 m/s reported by Wilkins [16]. In the plot at the top of Fig. 10, only the ballistic limit from the simulations using $\Psi = 0.5$ is more than a few percent greater than 660 m/s, suggesting that $\Psi = 0.5$ more closely represents SiC-B than $\Psi = 1.0$ or $\Psi = 0.75$.

4.0 Discussion and Conclusions

In this study, the Gudehus [7] form of dependence on the third invariant is incorporated into the yield surface of the JHB ceramic model. The model parameters for silicon carbide are modified to retain agreement with test data for several degrees of third-invariant dependence. The simulations of the previous sections show trends in the influence of the third invariant on the behavior of silicon carbide under high-velocity impact.

For rods impacting thick targets of silicon carbide, increasing the influence of the third invariant increases penetration depths by small or negligible amounts. In prestressed targets, this effect appears as a small decrease in the duration of dwell when impact velocities are in the range of dwell transitioning to penetration. In confined but non-prestressed targets, primary penetration depths increase by small amounts consistently over a broad range of impact velocities. In unconfined targets, the third invariant shows no discernable effect on the penetration velocity.

For small-caliber bullets impacting thin targets with aluminum substrates (and silicon-carbide thickness similar to bullet caliber), increasing the influence of the third invariant significantly increases the ballistic limit. This increase in performance is the opposite of that for thick targets.

In addition to identifying trends in the influence of the third invariant, it is also possible to infer the magnitude of the influence in silicon carbide. This can be done by comparing the simulations to test data. In the compressive plate-impact tests, reloading to yield in tension is best replicated by the simulations using $\Psi = 0.5$. And although the silicon carbide used in the ballistic tests of thin targets is not the SiC-B simulated in this study, it appears the simulated ballistic limit using $\Psi = 0.5$ provides best fidelity with the tests. In thick targets, the influence of the third invariant is too small relative to noise in the tests and simulations to infer the most appropriate influence. Therefore, it appears that the influence of the third invariant is significant in silicon carbide, but it is only manifested under certain loading conditions of high-velocity impact, such as those in thin targets and compressive plate impacts.

5.0 References

1. M. Polonco-Loria, O. S. Hopperstad, T. Borvik and T. Berstad. "Numerical predictions of ballistic limits for concrete slabs using a modified version of the HJC concrete model." *International Journal of Impact Engineering* **35**, pp. 290-303 (2008).
2. A. O. Frank, M. D. Adley and K. T. Danielson. "On the importance of a three-invariant model for simulating the perforation of concrete slabs." In: *78th Shock and Vibration Symposium*, Philadelphia, Pennsylvania (2007).
3. W. Riedel, K. Thoma, S. Hiermaier and E. Schmolinske. "Penetration of reinforced concrete by BETA-B-500 numerical analysis using a new macroscopic concrete model for hydrocodes." In: *9th International Symposium on Interaction of the Effects of Munitions with Structures*, Berlin, Germany (1999).
4. G. R. Johnson, T. J. Holmquist and S. R. Beissel. "Response of aluminum nitride (including a phase change) to large strains, high strain rates, and high pressures." *Journal of Applied Physics* **94**, p. 1639 (2003).
5. P. E. Senseny, A. F. Fossum and T. W. Pfeifle. "Non-associative constitutive laws for low porosity rocks." *Int J Num Anal Meth Geomech* **7**, pp. 101-115 (1983).
6. K. G. Willam and E. P. Warnke. "Constitutive model for the triaxial behavior of concrete." In: *Concrete structures subjected to triaxial stresses.* ISMES, Bergamo (1975).
7. G. Gudehus. "Elastoplastische stoffgleichungen fur Trockenen sand." *Ingenieur Arch* **42**, p. 151-169 (1973).
8. G. C. Nayak and O. C. Zienkiewicz. "Convenient forms of stress invariants for Plasticity." *Proceedings of the ASCE Journal of the Structural Division* **99** (ST4), pp. 949-954 (1972).
9. T. J. Holmquist and G. R. Johnson. "Characterization and evaluation of silicon carbide for high-velocity impact." *Journal of Applied Physics* **97**, 093502-1 (2005).
10. D. E. Grady and R. L. Moody. Report No. SAND96-0551, Sandia National Laboratory (1996).
11. D. P. Dandekar and P. T. Bartkowski. Report No. ARL-TR-2430, Army Research Laboratory (2001).
12. P. Lundberg, R. Renstrom, and B. Lundberg, "Impact of metallic projectiles on ceramic targets: transition between interface defeat and penetration," *Int. J. Impact Engng.,* **24**(3): 259-275 (2000).
13. D. L. Orphal and R. R. Franzen, "Penetration of confined silicon carbide targets by tungsten long rods at impact velocities from 1.5 to 4.6 km/s," *Int. J. Impact Engng.*, **19**(1): 1-13 (1997).
14. T. J. Holmquist, C. E. Anderson, Jr., T. Behner, D. L. Orphal. "The mechanics of dwell and post-dwell penetration." *Advances in Applied Ceramics* **108**, No. 8 (2010).
15. T. Behner, V. Hohler, C. E. Anderson, Jr., D. L. Orphal and D. W. Templeton. *Proceedings of the 21st International Symposium on Ballistics*, Adelaide, South Australia, p. 118 (Australia Press, 2004).
16. M. L. Wilkins. Report No. UCRL-50694, Lawrence Radiation Laboratory (1969).
17. G. R. Johnson and W. H. Cook. "A constitutive model and data for metals subjected to large strains, high strain rates, and high temperatures." In: *Seventh International Symposium on Ballistics*, The Hague, Netherlands (1983).
18. Y. V. Milman, S. I. Chugunova and I. I. Timofeeva. "The resistance of silicon carbide to static and impact local loading." *International Journal of Impact Engineering* **26**, pp. 533-542 (2001).

Appendix A: Damage Softening

This section examines the effects of damage softening in silicon carbide using a modified version of the original JHB ceramic model. As described previously, the strength of partially damaged material ($0 < D < 1$) is governed by the undamaged yield surface in the original JHB model. When damage is complete ($D = 1$), the strength is then governed by the damaged yield surface. As depicted in Fig. 1, the transition from the undamaged to the damaged yield surface occurs instantaneously.

It is possible that the strength of partially damaged material is not governed simply by the undamaged yield surface. In this section, two alternate descriptions are considered, and simulations are performed of the high-velocity impact tests using both of them. In the first alternate description, the yield surface is the undamaged yield surface until damage is halfway complete ($D = 0.5$); subsequently, it is interpolated linearly with damage between the undamaged surface at $D = 0.5$ and the fully damaged surface at $D = 1$. In the second alternate description, the yield surface is interpolated linearly with damage between the undamaged surface at $D = 0$ and the fully damaged surface at $D = 1$. This description is depicted in Fig. 1 by the dashed line labeled "gradual softening when $D > 0$." In the figures showing the simulation results, the original description of partially damaged yield strength is denoted, "soft = 0.0." The first alternate description is denoted, "soft = 0.5," and the second alternate description is denoted, "soft = 1.0." With this nomenclature, damage softening increases as parameter "soft" increases.

Figure A-1 shows the simulation and test results of the compressive plate impacts. For both impact velocities, there is virtually no difference between the velocity histories from soft = 0.0 and soft = 0.5, an indication that negligible damage accumulates beyond 0.5 in the silicon carbide. However, the velocity history from soft = 1.0 differs in loading, as the result of a slower inelastic wave speed. It also differs upon unloading and yield in tension, as the pullback signal is smaller. This difference brings the simulation in closer agreement with the test data.

Figure A-2 shows the simulation and test results of the tensile-spall plate impacts. Here there are insignificant differences between the three degrees of damage softening, as the yield surface is not reached (and damage is not accumulated) until the load is reversed and the material fails in tension.

Figure A-3 shows the simulation and test results of the long-rod impacts with prestressed targets. Significant differences are apparent in the duration of dwell for the 1410-m/s and 1645-m/s impact velocities. In particular, at 1410 m/s the case of soft = 0.0 fails to penetrate after at least 30 μs of dwell, while the case of soft = 1.0 dwells for only about 5 μs. At 2175 m/s, none of the simulations dwell and the penetration velocities are nearly identical.

Figure A-4 shows the normalized penetrations at 10 μs after impact from the simulations of long-rod impacts with confined silicon-carbide targets. One simulation was performed at each impact velocity and each method of damage softening, such that error bars indicating sensitivities to small perturbations are not incorporated. The data show increased penetration depths for increased damage softening at impact velocities of 1300 m/s, 1500 m/s and 2000 m/s, but no significant differences at the higher velocities of 3000 m/s and 4000 m/s. The reduced strength with increased damage softening is apparently only significant relative to inertial effects at the low impact velocities.

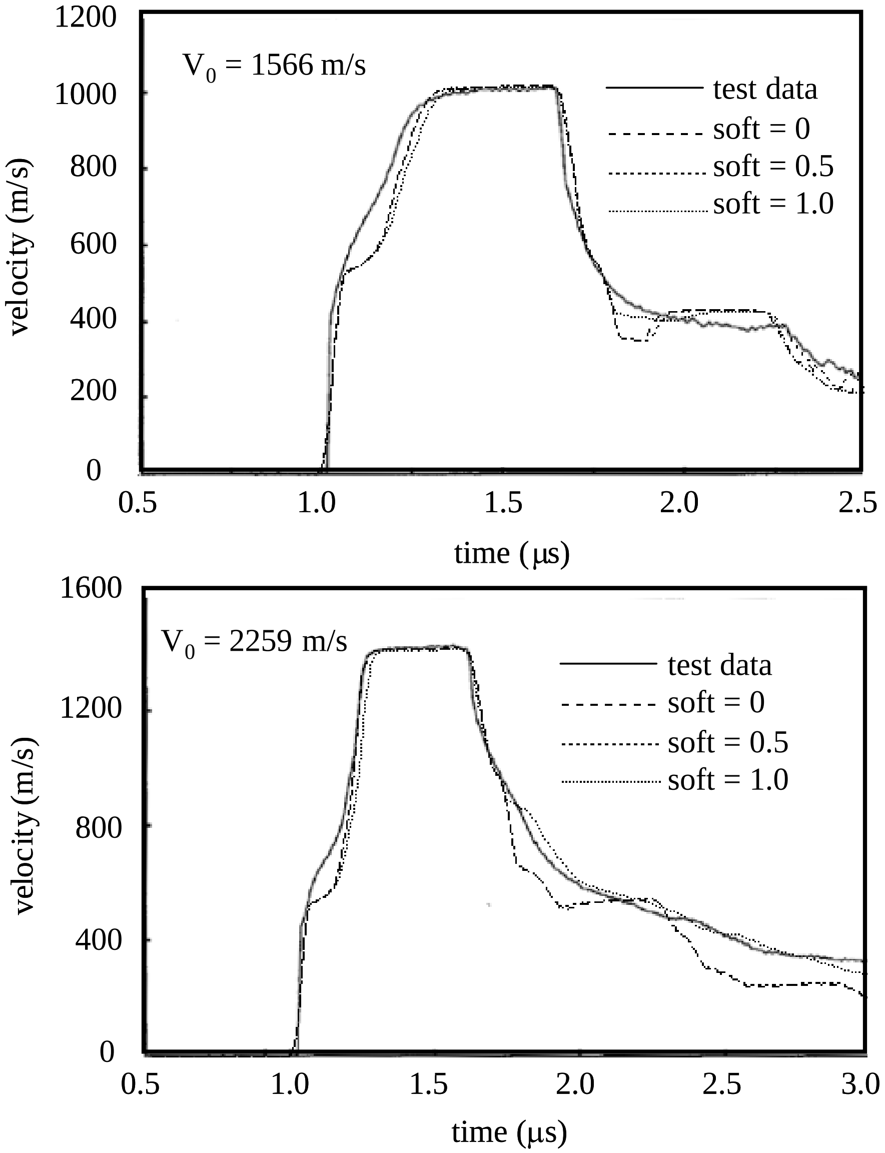

Figure A-1. Compressive plate-impact results from tests [10] and simulations for several degrees of damage softening and impact velocities of 1566 m/s (top) and 2259 m/s (bottom). Velocities are from the back surface of the silicon carbide.

Figure A-5 shows the simulated and test penetration velocities due to long-rod impacts of unconfined silicon-carbide targets. The simulation results show negligible influence of damage softening and good agreement with the test data.

Figure A-6 shows the residual velocities versus impact velocities from the simulations of small-caliber bullets impacting thin targets of silicon carbide with aluminum substrates. The data indicate a strong influence of damage softening on the ballistic limits, with the ballistic limit from soft = 1.0 about 100 m/s less than that from soft = 0.

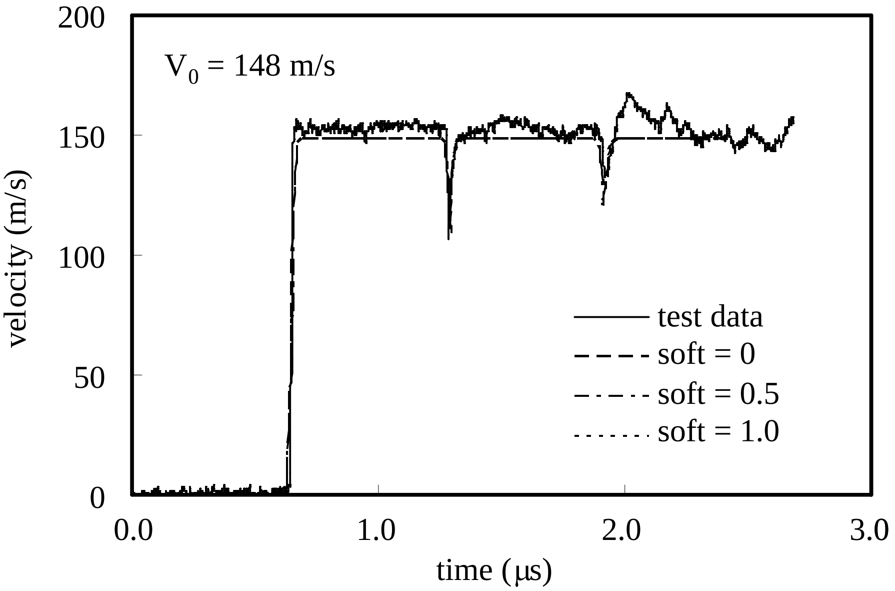

Figure A-2. Tensile-spall plate-impact results from the test [11] and simulations for several degrees of damage softening and an impact velocity of 148 m/s. Velocities are at the back surface of the silicon carbide.

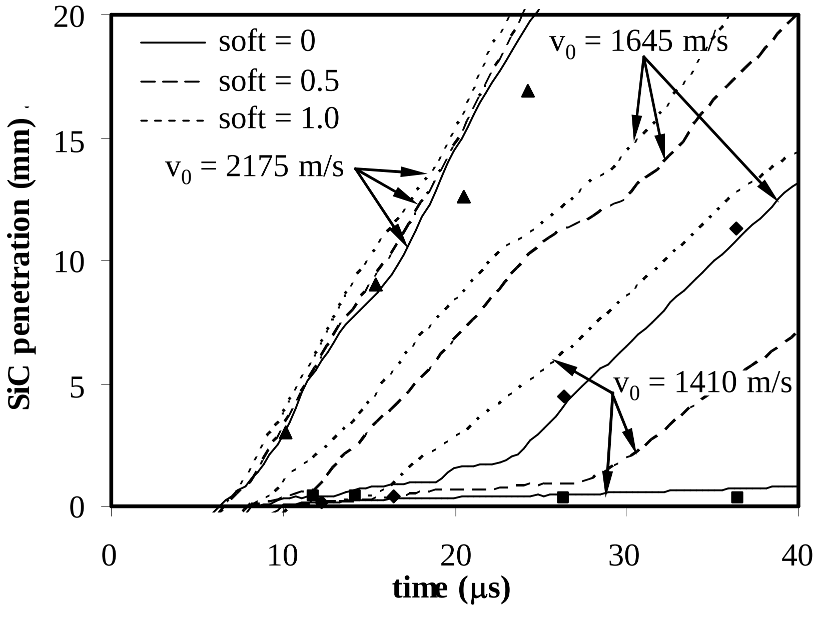

Figure A-3. Results of tungsten long-rod impacts with thick prestressed silicon-carbide targets from tests [12] and simulations for several degrees of damage softening. Test data are indicated by squares (1410 m/s), diamonds (1645 m/s) and triangles (2175 m/s).

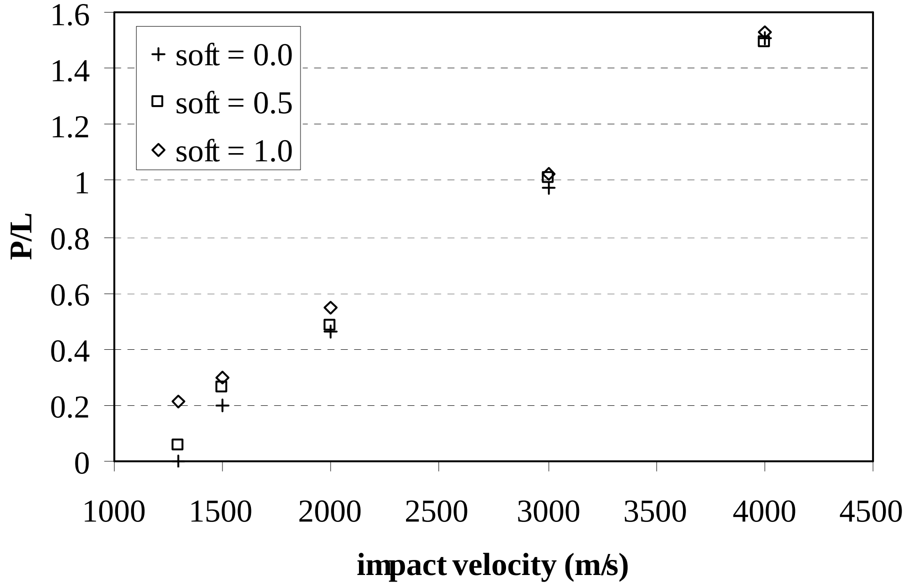

Figure A-4. Penetration depths from simulations of long-rod impacts with confined silicon-carbide targets for several degrees of damage softening.

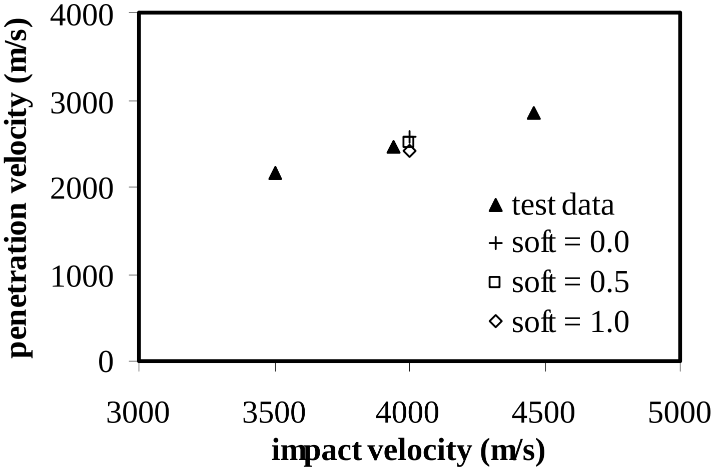

Figure A-5. Penetration velocities of long-rod impacts with unconfined silicon-carbide targets from tests [15] and simulations for several degrees of damage softening.

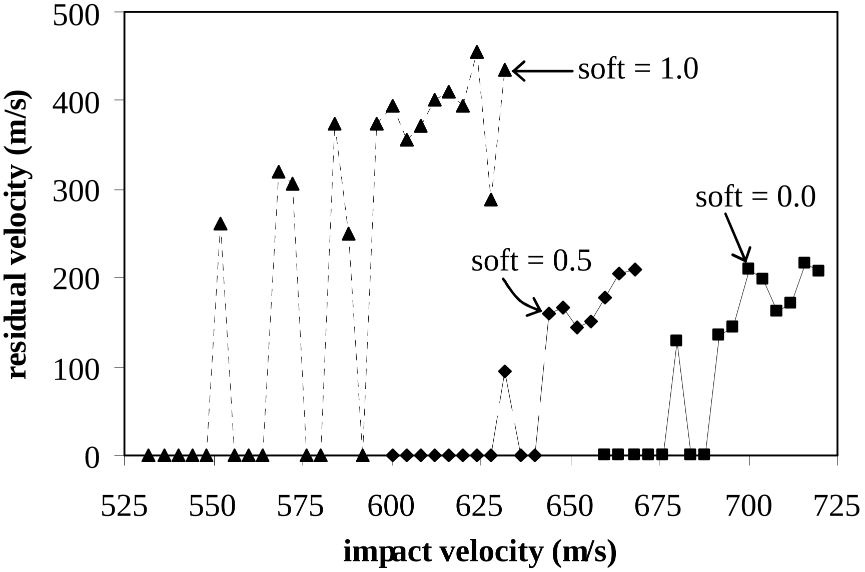

Figure A-6. Residual velocities from simulations of bullets impacting thin targets of silicon carbide and aluminum for several degrees of damage softening.

Appendix B: Thermal Softening

This section examines the effects of thermal softening in silicon carbide using a modified version of the original JHB ceramic model. Thermal softening has been accounted for by appending the factor $(1-T^{*m})$ onto the expression of the yield surface in Eqn. 1.

$$\sigma = \sigma_{TXC}(p;D)(1+C\ln\dot{\varepsilon}^{*})\,(1-T^{*m}) \tag{9}$$

In this expression, T^{*} is the homologous temperature, $T^{*} = (T - T_{room})/(T_{melt} - T_{room})$, and m is a model parameter. This factor reduces the strength from its value at room temperature, T_{room}, to zero at the melting temperature, T_{melt}, and its form has been adopted from the Johnson-Cook strength model for metals [17]. Indentation tests reported by Milman *et al* [18] of SiC-B at various temperatures have been used to find the model parameters for the simulations in this section: $m = 2.6$ and $T_{melt} = 1140\ K$. However, due to covalent bonding, the yield stress of silicon carbide as a function of temperature decreases sharply around its characteristic temperature of deformation, above which crystal lattice resistance to dislocation motion is greatly reduced. In addition, the function shows a sharp decrease near the much higher temperature of intensive sublimation, and it is relatively insensitive at other temperatures. The factor $(1-T^{*m})$ does not allow for inflection points, and the thermal softening of silicon carbide can therefore only be accurately modeled to about 600 degrees C. The model essentially neglects all strength above this temperature.

The uncertainty regarding the amount of internal-energy growth that contributes to increased temperatures has led to the inclusion of all internal energy in the temperature computations. This assumption, along with the aforementioned overestimate of thermal softening above about 600 C, reduces the simulations of this section to a high upper bound on the influence of thermal softening. In the figures, results from the model representing the upper bound on thermal softening are denoted by $m = 2.6$, and those neglecting thermal softening are denoted by $m = \infty$.

Figure B-1 shows the simulation and test results of the compressive plate impacts. For the impact velocity of 1566 m/s, the thermal softening results in a significantly reduced inelastic wave speed. For the impact velocity of 2259 m/s, thermal softening drastically reduces the inelastic wave speed, and also reduces the magnitude of the pullback signal upon reloading in tension.

Figure B-2 shows the simulation and test results of the tensile-spall plate impacts. Since the material remains elastic until it reaches the yield surface after reloading in tension, there are insufficient inelastic strains to activate thermal softening before failure.

Figure B-3 shows the simulation and test results of the long-rod impacts with prestressed targets. For the intermediate impact velocity of 1645 m/s, the 20 μs of dwell are completely eliminated by thermal softening. However, the duration of dwell at the 1410-m/s velocity is unaffected by the thermal softening, and the penetration velocity at the 2175-m/s impact velocity is marginally affected. These results reflect the highly unstable nature of the transition from dwell to penetration.

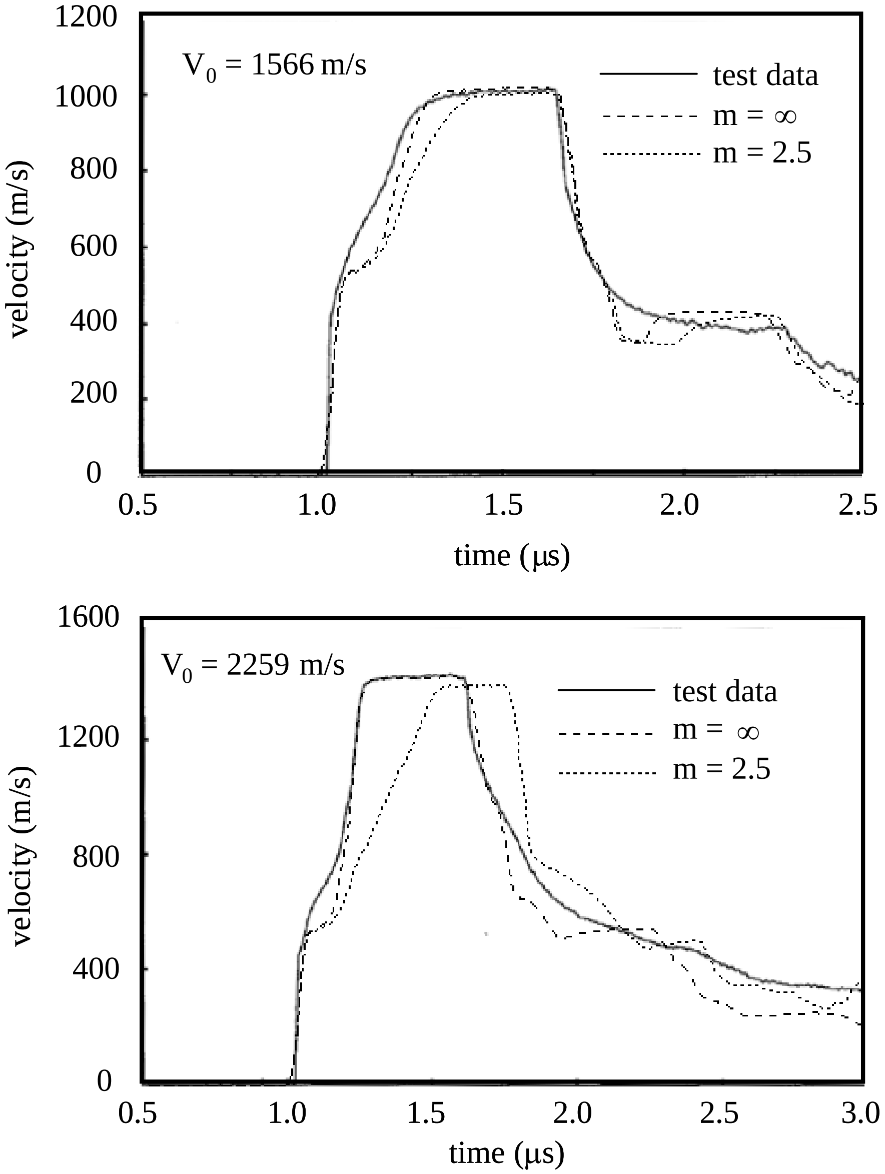

Figure B-1. Compressive plate-impact results from tests [10] and simulations with and without thermal softening at impact velocities of 1566 m/s (top) and 2259 m/s (bottom). Velocities are from the back surface of the silicon carbide.

Figure B-4 shows the normalized penetrations at 10 μs after impact from the simulations of long-rod impacts with confined silicon-carbide targets. One simulation was performed at each impact velocity for both degrees of thermal softening, such that error bars indicating sensitivities to small perturbations are not incorporated. As for damage softening, the thermal data indicate a clear trend toward reduced influence of softening as impact velocities increase. For the impact velocity of 1300 m/s, penetration occurs only with thermal softening; and for the impact velocity of 1500 m/s, penetration increases about 20 percent with thermal softening. For the higher impact velocities, the influence of thermal softening becomes negligible. The reduced yield strengths due to thermal softening are apparently only significant compared to inertial effects at the lower impact velocities.

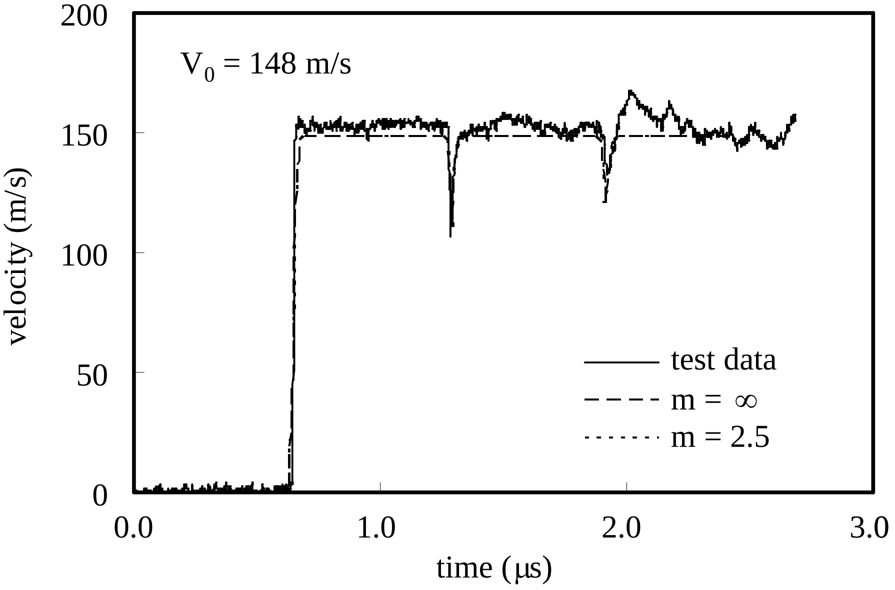

Figure B-2. Tensile-spall plate-impact results from the test [11] and simulations with and without thermal softening at an impact velocity of 148 m/s. Velocities are at the back surface of the silicon carbide.

Figure B-5 shows the simulated and test penetration velocities due to long-rod impacts of unconfined silicon-carbide targets. The simulation results show negligible influence of thermal softening and good agreement with the test data.

Figure B-6 shows the residual velocities versus impact velocities from the simulations of small-caliber bullets impacting thin targets of silicon carbide with aluminum substrates. Unlike damage softening, thermal softening shows no influence on the ballistic limit. The difference is perhaps due to the relatively small inelastic strains developed before failure on the back surface of the silicon carbide. Such strains are necessary to invoke thermal softening, while damage softening begins immediately upon yield for soft = 1.0.

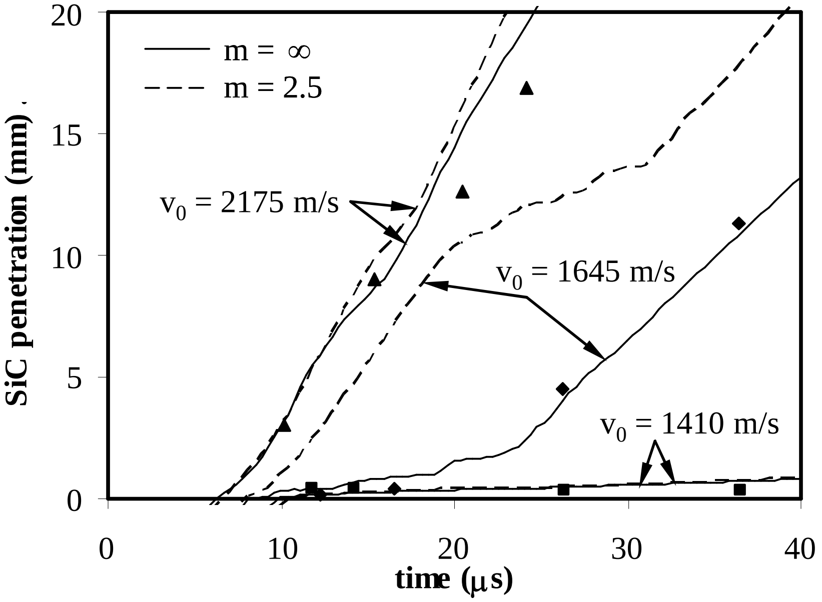

Figure B-3. Results of tungsten long-rod impacts with thick prestressed silicon-carbide targets from tests [12] and simulations with and without thermal softening. Test data are indicated by squares (1410 m/s), diamonds (1645 m/s) and triangles (2175 m/s).

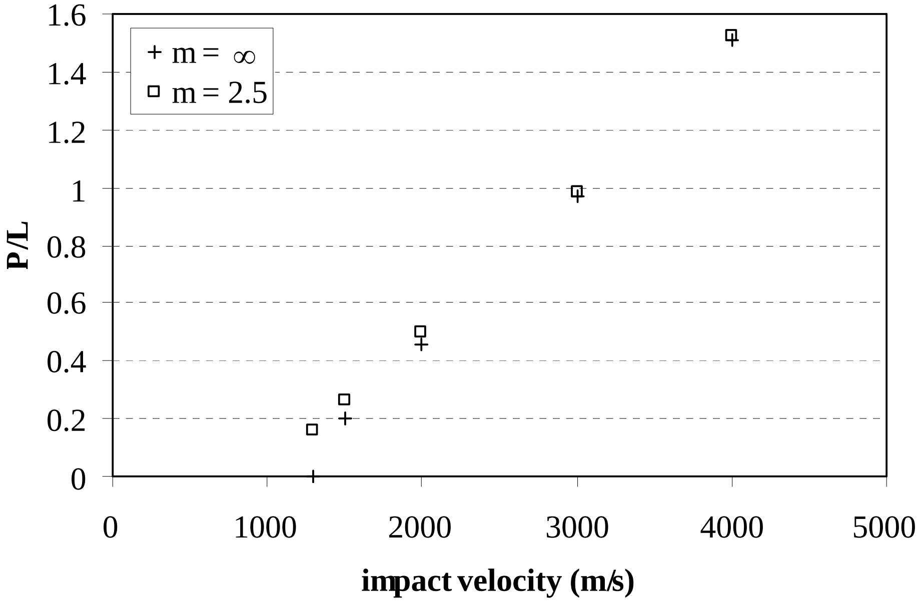

Figure B-4. Penetration depths from simulations of long-rod impacts with confined silicon-carbide targets with and without thermal softening.

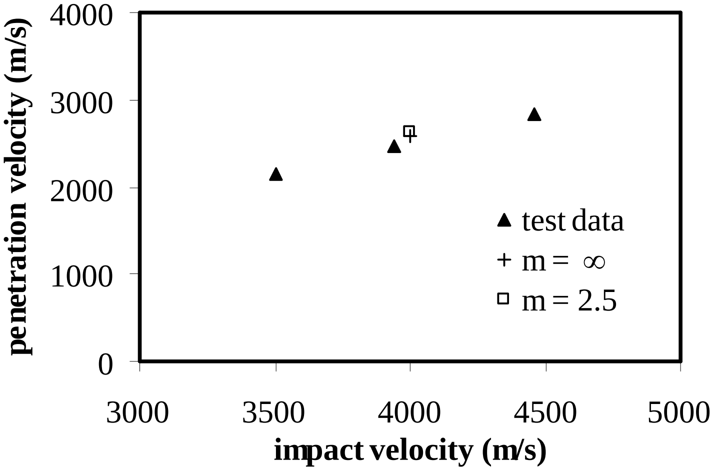

Figure B-5. Penetration velocities of long-rod impacts with unconfined silicon-carbide targets from tests [15] and simulations with and without thermal softening.

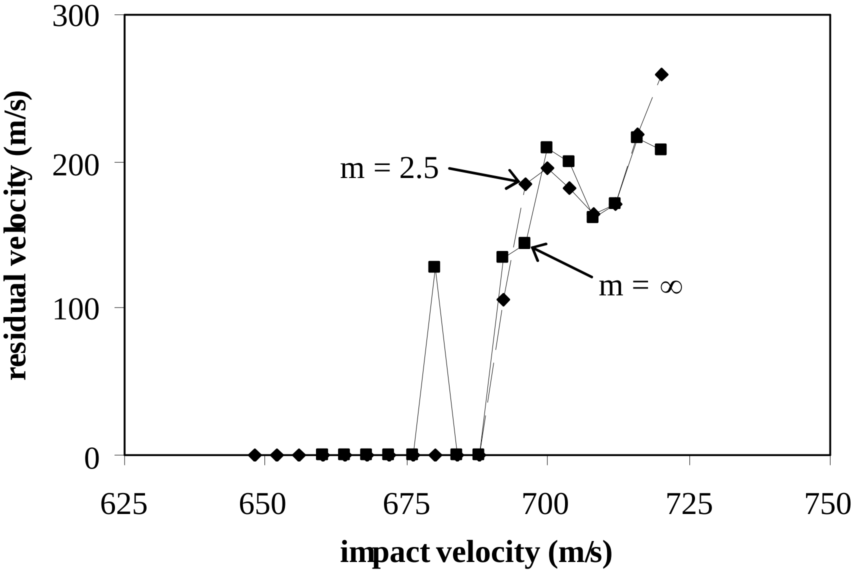

Figure B-6. Residual velocities from simulations of bullets impacting thin targets of silicon carbide and aluminum with and without thermal softening.